Microwave-Pumped Electric-Dipole Resonance Absorption for Noninvasive Functional Imaging

Wanling Luo,[†] Zhong Ji,[†] Sihua Yang, and Da Xing[*]
MOE Key Laboratory of Laser Life Science & Institute of Laser Life Science, College of Biophotonics, South China Normal University, Guangzhou 510631, China

(Received 1 December 2017; revised manuscript received 19 April 2018; published 28 August 2018)

Traditional microwave-induced thermoacoustic imaging is regarded as a structural imaging method that can recover the water content of biological tissues. Here, an alternative noninvasive functional imaging system based on microwave-pumped electric-dipole resonance absorption is reported. On the basis of the resonance principle, microwave radiation of a specific frequency can be used to selectively excite the polar molecules of interest. The microwave energy deposited creates an ultrasound disturbance through thermoelastic expansion. By detection of the ultrasound field, *in vivo* imaging of the target polar molecules with ultrasound resolution at the submillimeter level is realized. We show the thermoacoustic signal intensity of biological polar molecules with different electric dipole moments. We perform large-field-of-view thermoacoustic imaging of arterial and venous blood vessels *in vivo*, and find the thermoacoustic signal intensity increases synchronously on injection of exogenous polar molecules into the venous blood vessels of a rabbit ear. We also demonstrate the functional imaging capability of the thermoacoustic system in a study of the sensitivity of microwave absorption to changes in the concentration of polar molecules in the blood vessels of a rabbit ear. This imaging technique may find application in the detection of abnormal concentrations of biological polar molecules with large electric-dipole moments.

DOI: 10.1103/PhysRevApplied.10.024044

I. INTRODUCTION

Microwave-induced thermoacoustic imaging combines the advantages of the good image contrast of microwaves and the high resolution of ultrasound [1,2]. Traditional thermoacoustic imaging has been used to image biological structures on the basis of their water content [3] and has potential for early diagnosis of breast cancer [4,5] and detection of foreign objects [6,7]. Recently, our research group found that blood can produce stronger thermoacoustic signals than water. Our further studies showed that polar molecules other than water in blood contribute substantially to microwave absorption and the consequent production of thermoacoustic signals.

It is reported that blood contains 91%–92% water and other main components, such as proteins, inorganic salts, nonprotein nitrogen compounds, and saccharides. Some of these nutrients are polar molecules that possess a large electric-dipole moment [8–13] and play crucial roles in almost all biological processes. For example, in colon-cancer patients, serum arginine (Arg) concentrations are lower than in healthy people [14]. Glucose (Glu) is the primary energy source, particularly for brain cells. Both uptake and metabolism of Glu by the brain deteriorate in Alzheimer's disease [15]. Moreover, low serum albumin (Alb) concentration is an independent predictor of long-term mortality in breast cancer [16].

At present, the detection of biological polar molecules is mostly based on *ex vivo* chromatography or electrochemical analysis [17,18]. *In vivo*, ^{1}H magnetic resonance spectroscopy (^{1}H MRS) is a noninvasive and safe method to study the metabolic features associated with polar molecules [19,20]. However, breathing and peristalsis can lead to severe magnetic susceptibility difficulties in the detection of polar molecules and can also affect the local magnetic field homogeneity, which results in spectral line broadening or even loss of the signal [21]. Tumors located in the lungs, stomach, and gastrointestinal tract are difficult to analyze with ^{1}H MRS [22]. Therefore, a noninvasive and effective method to image the distribution of biological polar molecules *in vivo* is particularly necessary for molecular diagnostics and metabolism monitoring.

When subjected to external microwave radiation of an appropriate frequency, polar molecules will be oriented in the direction of the applied field [23]. In other words, a polar molecule of interest can be efficiently and selectively excited by the choice of a specific microwave frequency. Then, the polar molecules' spatial-density properties can be imaged with ultrasound resolution by

[*]xingda@scnu.edu.cn
[†]These authors contributed equally to this work

detection and reconstruction of the ultrasound field. Hence, this noninvasive functional imaging method does not have the limitation of local field fluctuation in ^{1}H MRS.

In this paper, we first analyze the resonance-absorption principle of polar molecules theoretically and then report the acquisition of thermoacoustic signals of biological polar molecules with different electric-dipole moments experimentally. Then we establish a thermoacoustic functional imaging system, and image arterial and venous blood vessels with a large field of view. Furthermore, by exploring the microwave-absorption characteristics of polar molecules in blood, we explain the reasons for the differences in microwave absorption between arterial and venous blood vessels. Finally, we use a method for monitoring the concentration changes of polar molecules in real time and achieve thermoacoustic functional imaging. The results indicate that the thermoacoustic functional imaging system may have potential to be used for real-time tracking of polar-molecule dynamics in abnormal tissues.

II. MATERIALS AND METHODS

A. Microwave-pumped electric-dipole resonance-absorption principle

The principle of the thermoacoustic effect is similar to that of photoacoustic imaging: both use pulsed electromagnetic waves as the excitation source and ultrasound waves as the information carrier [24–26]. When biological tissues are exposed to a microwave field, the absorbed microwave energy is usually partially or completely converted into heat through electromagnetic losses. Then, the heat energy is transformed into kinetic energy due to thermal confinement. Afterwards, the kinetic energy leads to tissue expansion and contraction, acting as a source of ultrasound waves. The ultrasound waves are detected outside the tissue by an ultrasonic transducer to form an image that maps the original microwave energy deposition inside the tissues. The electromagnetic losses mainly include magnetic hysteresis loss, ionic conductivity loss, and dipolar-polarization loss. For a sample of volume V, the power density produced by electromagnetic losses can be expressed as

$$P = \iiint_V (P_M + P_I + P_D)\, dV, \tag{1}$$

where P_M, P_I, and P_D are the average power density caused by the magnetic hysteresis loss, ionic conductivity loss, and dipolar-polarization loss, respectively. During magnetic hysteresis loss, the magnetic state of magnetic materials will change when they are exposed to an alternating magnetic field, and the intensity of magnetization lags behind the magnetic field strength. This phenomenon leads to magnetic hysteresis loss and generates heat energy due to the magnetocaloric effect [27,28]. In ionic conductivity loss the dissolved charged particles oscillate back and forth in response to the microwave irradiation and generate kinetic energy. Because of the viscous drag of the molecular electric field, the kinetic energy is dissipated, resulting in a loss component and eventually in heating [29]. For dipolar molecules, dipolar-polarization loss is induced by the oscillating field. When the applied electric field oscillates at a microwave frequency, the dipolar molecules will be oriented in the direction of the applied field [Fig. 2(b)], and the energy is converted to heat through molecular friction and collisions [30]. Because most nutrients in blood are polar molecules [Fig. 2(a)], the main discussion in this paper concerns microwave absorption due to dipolar polarization.

The average power density P_D absorbed from a field $E(t) = E_0 \sin(\omega t)$ is given by [31]

$$P_D = \frac{\omega}{2} \varepsilon_0 \varepsilon'' E_0^2, \tag{2}$$

where ω is the microwave frequency, ε_0 is the permittivity of a vacuum, ε'' is the dielectric loss, and E is the electric field. Hence, the average power density mainly depends on the dielectric loss when different samples are in the same microwave field.

The dielectric loss is described by Debye's dielectric relaxation theory, which yields Eq. (3) [32,33]:

$$\varepsilon'' = (\varepsilon_s - \varepsilon_\infty) \frac{\omega \tau_D}{1 + \omega^2 \tau_D^2}, \tag{3}$$

where ε_∞ is the permittivity at the limit of infinite frequency, ε_s is the permittivity under a static electric field, and τ_D is the relaxation time. To assess the electric-dipole moments of the solutes quantitatively, the Guggenheim approximation for dilute solutions is used [34,35]:

$$\mu^2 = \frac{27 \varepsilon_0 k_B T M_g \upsilon}{N_A (\varepsilon_m + 2)^2} \left(\frac{\partial \varepsilon_s}{\partial w_g} - \frac{\partial \varepsilon_p}{\partial w_g} \right), \tag{4}$$

realistically assuming $\partial \varepsilon_p / \partial w_g \approx 0$. In this equation, k_B is Boltzmann's constant, N_A is Avogadro's constant, ε_m is the permittivity of the medium (solvent), ε_p is the optical dielectric constant, M_g is the molar weight of the solutes, $\upsilon = 1/\rho$ is the specific volume of the solvent, and w_g is the weight fraction of the solute molecules. Combining Eqs. (3) and (4), we obtain the relationship between dielectric loss ε'' and electric dipole moment μ:

$$\varepsilon'' = \frac{n N_A (\varepsilon_m + 2)^2 \mu^2}{27 \varepsilon_0 k_B T} \frac{\omega \tau_D}{1 + \omega^2 \tau_D^2}. \tag{5}$$

The concentration, n, is in moles per unit volume. Equation (5) shows that the dielectric loss contribution reaches a maximum at a resonance frequency where the applied field

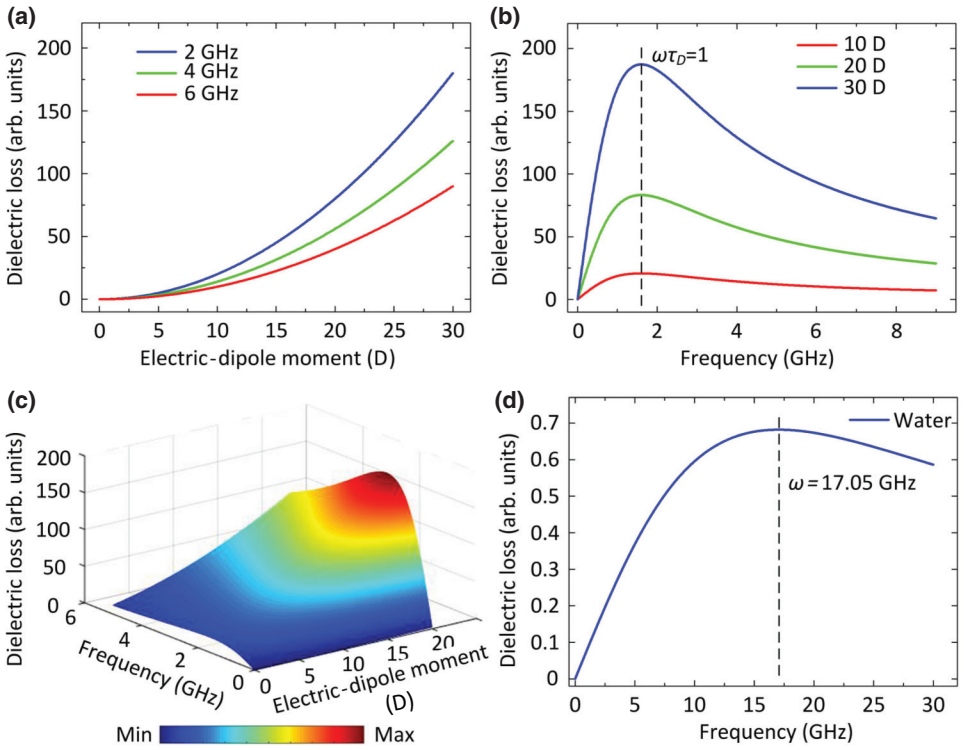

FIG. 1. Microwave-pumped electric-dipole resonance phenomenon. (a) Numerical calculation of dielectric loss for polar molecules with different frequencies (2, 4, and 6 GHz). (b) Numerical calculation of dielectric loss for polar molecules with different electric-dipole moments (10, 20, and 30 D). (c) Numerical calculation of electric-dipole resonance loss. (d) The dielectric loss peak for water is 17.05 GHz at 20 °C.

has the same period as the relaxation process ($\omega\tau_D = 1$) [33]. Additionally, the dielectric loss of polar molecules is proportional to the square of the electric-dipole moment. Therefore, polar molecules with a larger electric-dipole moment will absorb more microwave energy than those with a smaller electric-dipole moment.

The parameters in the numerical calculations are listed in Table I and the results of the numerical calculation with Eq. (5) are shown in Fig. 1. Figure 1(a) shows the results of numerical calculation of the dielectric loss for polar molecules with different frequencies (2, 4, and 6 GHz). It is clear that the dielectric loss of a polar molecule is larger at lower microwave frequency than at a higher frequency when the relaxation time is 100 ps. The results of the numerical calculation of the electric-dipole resonance absorption are shown in Figs. 1(b) and 1(c). The resonance loss is visible at 1.6 GHz when the relaxation time is 100 ps. Also, the loss increases by 9 times when the electric-dipole moment increases from 10 to 30 D [Fig. 1(b)], which approximates a quadratic dependence on the electric-dipole moment. A water molecule, whose dielectric loss is shown in Fig. 1(d), is the most common kind of polar molecule. The loss peak appears at 17.05 GHz when the relaxation time is 9.39 ps [36].

B. Experimental setup

To verify the resonance principle described in the previous section, a two-dimensional-scanning thermoacoustic imaging system is used, as shown in Fig. 2(a). A 6-GHz microwave generator (BW-6000HPT; Northmicro Electromechanical Technology, Xi'an, China) transmits 0.5-μs microwave pulses at a repetition frequency of 10 Hz controlled by a computer that can transmit synchronous pulses. The microwave peak power is 350 kW. The size of the waveguide output for microwave radiation is $\pi \times 3.2^2$ cm^2, so the energy density per unit area is $E \approx (350 \times 0.5)/(\pi \times 3.2 \times 3.2) = 5.44$ mJ/cm^2. The samples are placed in a plastic box that is immersed in mineral oil to couple thermoacoustic waves and is fixed in the microwave shield room to remain stationary. The thermoacoustic signals are received by a linear multielement transducer (128 elements; L2L50A; Shantou Institute of Ultrasonic Instruments Ltd., Shantou, China) with a scanning width of 52 mm centered at a frequency of 2.5 MHz with a nominal bandwidth of 70%. The signals from each element are transmitted, amplified, filtered, converted, and cached by a data-acquisition system. The data-acquisition system mainly consists of two 32-channel acquisition cards (5752; National Instruments, USA) with a sampling rate of 50 MHz. The frequency response of the thermoacoustic signal is 3.28 MHz (see Fig. S5 in the Supplemental Material [37]). Finally, the acquired signals are transferred to a computer for reading peak-to-peak values and reconstructing a two-dimensional image by use of a maximum-intensity-projection algorithm. In this system, the lateral resolution is 0.80 mm and the axial resolution is 0.84 mm (see Fig. S4 in the Supplemental Material [37]).

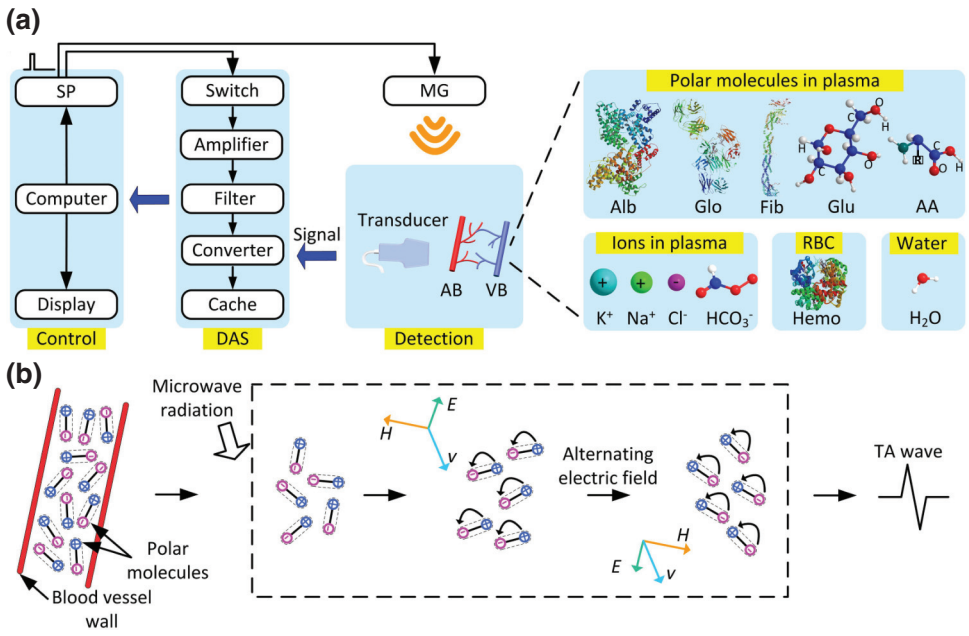

FIG. 2. The experimental setup of the thermoacoustic (TA) imaging system and the principle of microwave-pumped electric-dipole resonance absorption. (a) The experimental setup of the TA imaging system, and a variety of biological components in the arterial blood (AB) and venous blood (VB) vessels. Alb, Protein Data Bank (PDB) entry 1AO6; Glo, PDB entry 1IGT); Fib, PDB entry 3GHG); hemoglobin (Hemo), PDB entry 2H35. (b) The principle of microwave-pumped electric-dipole resonance absorption. AA, amino acid; DAS, data-acquisition system; MG, microwave generator; RBC, red blood cell; SP, synchronous pulses.

III. RESULTS

A. Thermoacoustic signals of polar molecules with different electric-dipole moments

Equation (5) shows that the dielectric loss of polar molecules is proportional to the square of the electric-dipole moment and polar molecules with a larger electric-dipole moment will absorb more microwave energy than those with a smaller electric-dipole moment. To verify this theory, nine biological polar molecules in aqueous solutions (0.5 mol/l) with different electric-dipole moments are measured. The polar molecules are L-threonine (Thr), L-serine (Ser), L-proline (Pro), L-valine (Val), L-alanine (Ala), L-glycine (Gly) (CapitalBio Corporation, Shanghai, China), L-Arg, L-lysine (Lys) (Macklin Biochemical, Shanghai, China), and edible Glu (Fengyizushi, Guangzhou, China). The electric-dipole moments of the polar molecules are summarized in Table II.

In the experiment, to exclude the influences of sample shapes, microwave energy, and transducer position, equipment composed of a transducer, a transparent plastic tube (2 mm in diameter), and a plastic box filled with mineral oil to couple thermoacoustic waves is made. The plastic tube and box are examined to confirm they have no microwave absorption. This equipment has a fixed geometry so as to keep the ultrasonic transmission efficiency constant. The biological polar molecules are injected in the plastic tube and illuminated by microwaves to acquire thermoacoustic signals, and the plastic tube is rinsed with distilled water before each injection to keep it clean. Experimental results are shown in Table II. Figure 3 clearly shows the differences in thermoacoustic intensity between the various polar molecules. From Fig. 3, we can see that the normalized thermoacoustic signal intensity of polar molecules with a larger electric-dipole moment is stronger than that of those with a smaller electric-dipole moment.

B. Thermoacoustic imaging of arterial and venous blood *in vitro*

To verify the thermoacoustic imaging capability for blood vessels, simulated experiments *in vitro* are performed. Four groups of mimic arterial and venous blood vessels are studied [Fig. 4(b)]. The arterial and venous blood come from rabbit ears (adult New Zealand white rabbits); 0.45 ml of blood is extracted each time and mixed with 0.05 ml of an anticoagulant (ethylenediaminetetraacetic acid disodium salt; Sangon Biotech, Shanghai, China). In the experiment, the plastic tubes filled with whole blood are illuminated with microwaves and flatted on the sample stage. The plastic tubes are 1 cm long and two plastic tubes are separated by 3 mm. The thermoacoustic signals produced are received by a transducer that is driven by two stepper motors for the two-dimensional scanning. The scanning time is about 2000 s (an image with 128×100 pixels, a total of 100 acquisition steps

TABLE I. Parameters in the numerical calculations.

n (mol/l)	N_A (mol^{-1})	ε_m (F/m)	ε_0 (F/m)	k_B (J/K)	T (K)	τ_D (s)
1	6.02×10^{23}	80.18	8.85×10^{-12}	1.38×10^{-23}	293.15	1×10^{-10}

TABLE II. The molecular weight, electric-dipole moments, and thermoacoustic signal intensity of various polar molecules.

	Lys	Arg	Gly	Ala	Val	Pro	Ser	Glu	Thr	Water
MW	146.19	174.2	75.07	89.09	117.15	115.13	105.09	180.16	119.12	18
EDM	16.2[a,b]	14.1[a,b]	11.50[c]	11.04[c]	10.80[c]	10.5[b]	10.34[b]	10[d]	9.80[b]	1.85[e]
TA	1.412	1.342	1.293	1.263	1.252	1.248	1.241	1.182	1.144	1
SD	0.045	0.036	0.011	0.017	0.036	0.015	0.021	0.031	0.026	0.009

MW, molecular weight; EDM, electric-dipole moment (debyes); TA, thermoacoustic signal intensity; SD, standard deviation.
[a]From Ref. [8].
[b]From Ref. [9].
[c]From Ref. [10].
[d]From Ref. [11].
[e]From Ref. [12].

are acquired with an average of 100 times per step). A schematic diagram is shown in Fig. 4(a).

Figure 4(b) shows that the reconstructed thermoacoustic images of blood vessels. For quantitative analysis, the dotted white lines selected in the four thermoacoustic reconstructed images have the same coordinates [Fig. 4(b)]. According to the statistical results from lines C1 and C2, the mean pixel value of arterial blood is 8.45% higher than that of venous blood. From lines C3 and C4, the mean pixel value of arterial blood is 8.53% higher than that of venous blood [Fig. 4(c)]. The results indicate that there are components with specific absorption in blood, and the content of the components is different in arterial and venous blood. In addition, the differences in absorption of arterial and venous blood can be recognized in the thermoacoustic images. Thus, thermoacoustic deep-blood-vessel imaging can be achieved with a spatial resolution at the submillimeter level on a centimeter scale [2,3].

C. Thermoacoustic signals of plasma components

To obtain a detailed analysis of the thermoacoustic signal intensity of plasma components, eight kinds of main components that are relatively abundant or whose electric-dipole moments are relatively large in plasma are detected with use of the same microwave energy density with concentrations of 10, 20, 30, 40, 50, and 60 mg/ml in aqueous solutions. The experimental results are shown in Fig. 5(a). The measured components are human serum Alb (Xiya Reagent, Linyi, China), γ-globulin (Glo) in cattle serum (AIKE Reagent, Chengdu, China), fibrinogen (Fib) from human plasma (Sigma-Aldrich, St. Louis, Missouri, USA), NaCl (Macklin Biochemical, Shanghai, China), Lys, Arg, Gly, and edible Glu. As can be seen in Fig. 5(a), the thermoacoustic signals of the eight kinds of components are much higher than that of water and the microwave absorption of different components is also different.

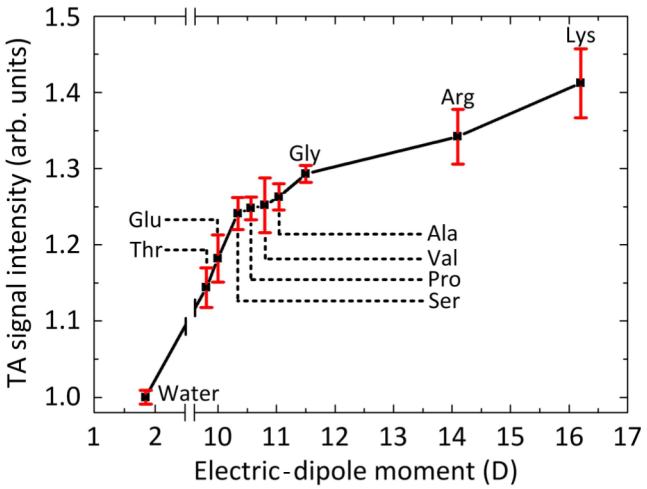

FIG. 3. The normalized thermoacoustic (TA) signal intensity of the biological polar molecules in aqueous solutions (0.5 mol/l).

To determine the contribution of different components to the microwave absorption in venous blood plasma, the thermoacoustic signal intensity of plasma components at a concentration of 60 mg/ml [Fig. 5(a)] and that of the normal content of each component in venous blood plasma are used. The normal content of each component in venous blood plasma is as follows (mean $\pm$ standard deviation): Alb, 46.60 ± 0.60 mg/ml [38]; Glo, 34.00 ± 6.00 mg/ml [39]; Fib, 3.26 ± 0.93 mg/ml [40]; Glu, 0.89 ± 0.09 mg/ml [41]; Na^+, 3.08 ± 0.01 mg/ml; Cl^-, 3.44 ± 0.01 mg/ml [42]; Lys, 0.025 ± 0.009 mg/ml; Arg, 0.014 ± 0.005 mg/ml; Gly, 0.021 ± 0.008 mg/ml [43]. In addition, the microwave-absorption ability can be calculated from the thermoacoustic signal intensity for unit concentration. From comparison with the normalized thermoacoustic signal intensity of venous blood plasma, the normalized contribution of venous-blood-plasma components can be calculated. Figure 5(b) shows the main contribution to microwave absorption is from polar molecules, especially Alb and Glo.

Moreover, the microwave-absorption ability of arterial blood is greater than that of venous blood. The crucial reason is that arterial blood generally has higher concentrations of nutrients (mainly polar molecules) relative to venous blood [44]. For instance, it is widely believed that the content of Glu in arterial blood is 0.03–0.05 mg/ml

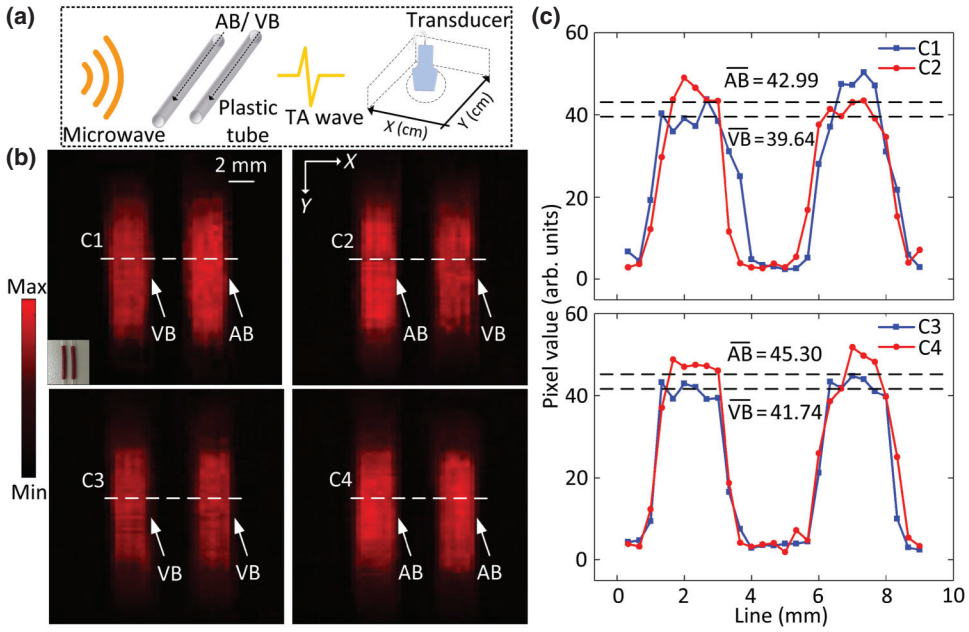

FIG. 4. The thermoacoustic (TA) imaging of arterial blood (AB) and venous blood (VB) *in vitro*. (a) The TA imaging system. (b) The TA images of mimic AB and VB vessels in various combinations. The inset shows the corresponding photograph. (c) The pixel values of lines C1, C2, C3, and C4 in (b). $\overline{AB}$ and $\overline{VB}$ represent the mean pixel value.

higher than in venous blood in the fasting state and the difference increases to 0.20–0.80 mg/ml after the administration of dextrose [45].

D. Monitoring of the concentration changes of polar molecules *in vivo*

To confirm that arterial and venous blood vessels *in vivo* can be distinguished by this system, a large-field-of-view image *in vivo* of blood vessels in rabbit ears is examined. Before the experiment, 2% pentobarbital sodium (Sigma-Aldrich, St. Louis, Missouri, USA) (1 ml/kg) is slowly injected into the ear marginal vein to narcotize the rabbit. Then the four legs of the rabbit are affixed to an iron shelf and the ear is covered with ultrasonic coupling liquid (Minhao Technology, Shenzhen, China) to reduce acoustic mismatch, which leads to surface reflection. In the thermoacoustic imaging experiments, the rabbit ear is placed under a box (no microwave absorption) that is filled with mineral oil and the transducer is submerged in the box. When the rabbit ear is irradiated by the pulsed microwaves, the thermoacoustic signals produced are received by the transducer, which is driven by two stepper motors for the two-dimensional scanning with a field of view of 5×4 cm^2. The experimental setup is illustrated in Fig. 6(a) and the results are shown in Fig. 6(b). To quantitatively analyze the microwave-absorption ability of arterial and venous blood, Fig. 6(c) plots the intensity profile of a cross-section image along line C in Fig. 6(b), and the maximum pixel values of arterial and venous blood in line C can be acquired. Figure 6(c) shows the maximum pixel values of arterial blood vessels are 8.43% and 9.70%, respectively, higher than those of venous blood vessels.

To verify that the thermoacoustic imaging system can monitor the concentration changes of polar molecules in blood in real time, the exogenous polar molecules are injected into the venous blood vessels of a rabbit ear. In the thermoacoustic signal experiments, Lys, Glu, and Glo at a concentration of 60 mg/ml in venous blood plasma solutions are slowly injected into the ear marginal venous

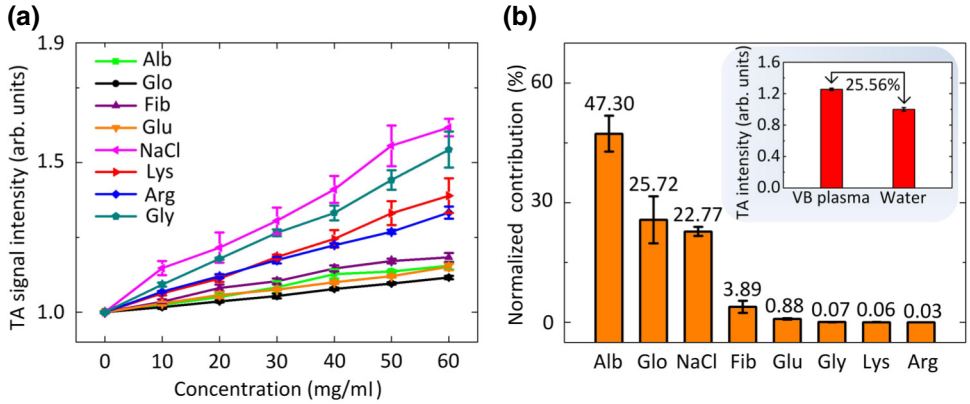

FIG. 5. The normalized thermoacoustic (TA) signal intensity and contribution of the main plasma components. (a) The normalized TA signal intensity of the biological molecules at different concentrations. (b) The normalized contribution from the microwave absorption of the main components in venous blood (VB) plasma. The inset shows the normalized TA signal intensity of VB plasma.

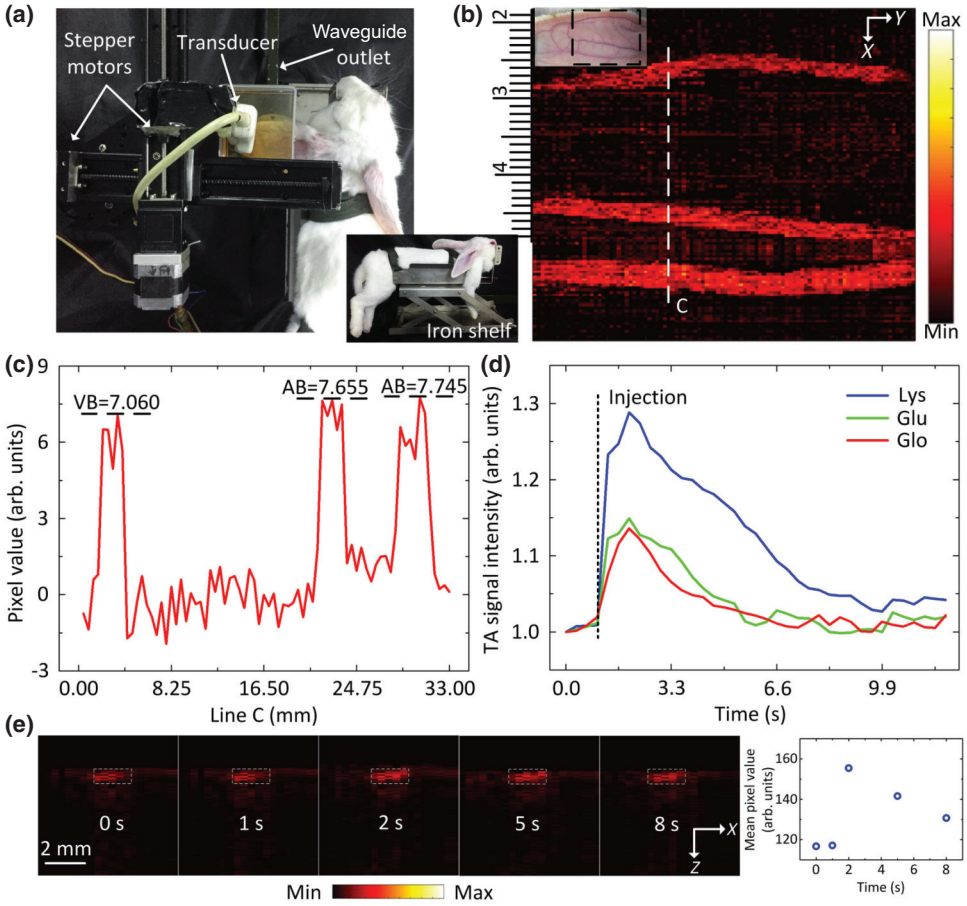

FIG. 6. The thermoacoustic (TA) functional imaging and TA signal intensity of blood vessels *in vivo*. (a) The experimental setup of the TA imaging system *in vivo*. The inset shows a photograph of the iron shelf. (b) Large-field-of-view TA imaging of arterial blood (AB) and venous blood (VB) vessels in the rabbit ear. The inset shows a photograph of rabbit ear. (c) The pixel values of line C in (b). (d) The normalized TA signal intensity after injection of Lys, Glu, and Glo at a concentration of 60 mg/ml in VB plasma solutions into the ear marginal VB vessels. (e) Real-time TA functional imaging of VB vessels when Lys is injected. The scatter diagram shows the mean pixel value of rectangular areas.

blood vessels to observe the change of thermoacoustic signals. In Fig. 6(d), the thermoacoustic signal intensity of venous blood is seen to increase greatly after injection of Lys, Glu, and Glo, and then falls over time. In Fig. 6(e), the functional imaging of the venous blood vessels is shown. When Lys is injected into the ear marginal venous blood vessels, the thermoacoustic signals are received by the transducer at different times. The mean pixel values of rectangular areas are counted [scatter diagram in Fig. 6(e)]. From the results we can see that the changing trend of the images [Fig. 6(e)] is consistent with the trend of the signals [Fig. 6(d)] when Lys is injected. These phenomena suggest that thermoacoustic functional imaging may have the potential for disease surveillance by monitoring the concentration changes of polar molecules in abnormal tissues.

E. Deep-blood-vessel imaging *in vivo*

The penetration of microwaves is superior to that of visible and near-infrared light [3,46,47]; thus, thermoacoustic imaging could be a deep-imaging technology. To demonstrate this imaging system can achieve deep-tissue imaging, thermoacoustic deep-blood-vessel imaging of the rabbit abdomen *in vivo* is performed. Before the experiments, the rabbit is in a drugged state, and the abdominal

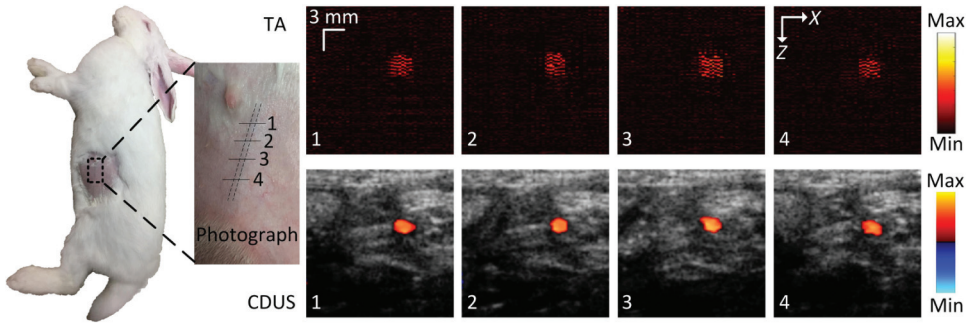

FIG. 7. The thermoacoustic imaging (top) and color Doppler ultrasound (CDUS) imaging (bottom) of a deep blood vessel in the rabbit abdomen. The enlarged image on the left is a photograph of the rabbit abdominal blood vessel.

area is shaved and depilated, and is covered with ultrasonic coupling liquid to reduce acoustic attenuation. Then, the rabbit is laid flat on the sample stage and the abdomen is illuminated by microwaves. The transducer is attached to the abdominal blood vessel for deep imaging. The results are shown in Fig. 7. The four images (1, 2, 3, and 4) correspond to four different parts of the abdominal blood vessel. Further, color Doppler ultrasound imaging is also displayed in Fig. 7 to support the thermoacoustic imaging. The results demonstrate that the locations of the abdominal blood vessel in color Doppler ultrasound imaging and thermoacoustic imaging are well correlated. Moreover, Fig. 7 indicates that this system can image deep tissue and provide an alternative approach for thermoacoustic functional imaging for practical application in tumor detection.

IV. DISCUSSION

The thermoacoustic functional imaging system based on the microwave-pumped electric-dipole resonance absorption principle discussed in this paper can be used to image tissues at a depth of a dozen centimeters by selection of the appropriate microwave wavelength [3]. On the one hand, although the tissues are irradiated by microwave pulses, the final image is reconstructed by the ultrasound signals, so our system can achieve the resolution of ultrasound imaging. On the other hand, the absorption characteristics of microwave energy are obviously different in various tissues, so the thermoacoustic imaging has high contrast. Because of the different concentrations of polar molecules in arterial and venous blood, we can distinguish arterial and venous blood vessels by thermoacoustic imaging. Additionally, the growth of abnormal tissues may lead to concentration changes of polar molecules [14–16]. Hence, polar molecules in blood with strong microwave absorption lay the foundation for monitoring patients with abnormal tissues. In summary, our system has the advantages of safety, comfort, low cost, and ease of operation, and it can also be applied for the early detection of diseases.

Several deficiencies in the current thermoacoustic functional imaging system are evident in the course of image-quality evaluation. Firstly, only one frequency is used to irradiate samples and thus the absorption of each component is difficult to distinguish. A possible solution is to use multiple or sweep microwave frequencies to excite samples, and then find the corresponding absorption peak and characteristic absorption waveforms of each component to obtain the concentrations of each component. Secondly, the in-plane resolution of 800 μm needs to be improved. A probable solution is to use a high-frequency detector, but the improvement of imaging resolution is almost at the expense of imaging depth, or in other words, the imaging depth must be reduced to obtain a high-resolution image. Lastly, the present method shows the ability of *in vivo* vascular imaging, while the speed of data acquisition remains a challenge. More experiments should be performed to improve the real-time vascular-imaging-reconstruction capability using the parallel data-acquisition system, but the problem of matching between multiple-acquisition cards needs to be solved.

V. CONCLUSIONS

We establish a thermoacoustic functional imaging system based on the microwave-pumped electric-dipole resonance-absorption principle that can image *in vivo* blood vessels of a rabbit ear. We reveal the specificity of arterial and venous blood vessels on the basis of the microwave-absorption differences of polar molecules in blood, and in real time monitor the concentration changes of polar molecules in blood. This system has great potential for clinical routine disease screening by monitoring the concentration changes of polar molecules in blood.

ACKNOWLEDGMENTS

This research was supported by the National Natural Science Foundation of China (Grants No. 61627827, No. 81630046, No. 61331001, and No. 91539127), the National High Technology Research and Development Program of China (Grant No. 2015AA020901), the Science and Technology Planning Project of Guangdong Province, China (Grants No. 2015B020233016, No. 2014B020215003, No. 2014A020215031, and No. 2017A020215135), the Young Teachers Scientific Research Cultivating Fund of South China Normal University (Grant No. 16KJ05), the China Postdoctoral Science Foundation (Grants No. 2017M610533 and No. 2018T110878), the Foundation for Distinguished Young Talents in Higher Education of Guangdong, China (Grant No. 2016KQNCX034), and the Science and Technology Program of Guangzhou, China (Grant No. 201804010432).

[1] H. Nan, B. A. Haghi, and A. Arbabian, Interferogram-based breast tumor classification using microwave-induced thermoacoustic imaging, IEEE Eng. Med. Biol. **2015**, 2717 (2015).

[2] C. Lou, S. Yang, Z. Ji, Q. Chen, and D. Xing, Ultrashort Microwave-Induced Thermoacoustic Imaging: A Breakthrough in Excitation Efficiency and Spatial Resolution, Phys. Rev. Lett. **109**, 218101 (2012).

[3] Z. Ji, C. Lou, S. Yang, and D. Xing, Three-dimensional thermoacoustic imaging for early breast cancer detection, Med. Phys. **39**, 6738 (2012).

[4] H. Ke, T. N. Erpelding, L. Jankovic, C. Liu, and L. V. Wang, Performance characterization of an integrated ultrasound, photoacoustic, and thermoacoustic imaging system, J. Biomed. Opt. **17**, 056010 (2012).

[5] S. Liu, Z. Zhao, X. Zhu, Y. Lu, B. Wang, Z. Nie, and Q. H. Liu, Block based compressive sensing method of microwave induced thermoacoustic tomography for breast tumor detection, J. Appl. Phys. **122**, 024702 (2017).

[6] L. Nie, D. Xing, and S. Yang, *In vivo* detection and imaging of low-density foreign body with microwave-induced thermoacoustic tomography, Med. Phys. **36**, 3429 (2009).

[7] Z. Chi, Y. Zhao, L. Huang, Z. Zheng, and H. Jiang, Thermoacoustic imaging of rabbit knee joints, Med. Phys. **43**, 6226 (2016).

[8] N. Agnihotri and P. C. Mishra, Hybridization-displaced charges for amino-acids: A new model using two point charges per atom along with bond-center charges, J. Mol. Model. **17**, 1435 (2011).

[9] M. K. Khoshkbarchi and J. H. Vera, A simplified perturbed hard-sphere model for the activity coefficients of amino acids and peptides in aqueous solutions, Ind. Eng. Chem. Res. **41**, 4319 (1996).

[10] K. Tamura, T. Ichiryu, J. Takemasa, and H. Li, Solubilities of mixed amino acids dissolved in water, APCChE **2004**, 315 (2004).

[11] R. N. Alfimova, N. A. Andreeva, N. I. Khoroshikh, and Y. L. Shishkin, Rotation of molecular fragments about bonds and the dipole moment of glucose and the Amadori rearrangement products of glucose, J. Struct. Chem. **15**, 830 (1975).

[12] M. B. Burt and T. D. Fridgen, Heterogeneous proton-bound dimers with a high dipole moment monomer: How could we experimentally observe these anomalous ionic hydrogen bonds, J. Phys. Chem. A **111**, 10738 (2007).

[13] E. Calabrò and S. Magazù, Parallel β-sheet vibration band increases with proteins dipole moment under exposure to 1765 MHz microwaves, Bioelectromagnetics **37**, 99 (2016).

[14] Y. L. Vissers, C. H. Dejong, Y. C. Luiking, K. C. Fearon, M. F. Meyenfeldt, and N. E. Deutz, Plasma arginine concentrations are reduced in cancer patients: Evidence for arginine deficiency, Am. J. Clin. Nutr. **81**, 1142 (2005).

[15] S. C. Cunnane, A. Courchesne-Loyer, V. St-Pierre, C. Vandenberghe, T. Pierotti, M. Fortier, E. Croteau, and C.-A. Castellano, Can ketones compensate for deteriorating brain glucose uptake during aging? Implications for the risk and treatment of Alzheimer's disease, Ann. N.Y. Acad. Sci. **1367**, 12 (2016).

[16] B. N. Azab, V. R. Bhatt, S. Vonfrolio, R. Bachir, V. Rubinshteyn, H. Alkaied, A. Habeshy, J. Patel, A. I. Picon, and S. W. Bloom, Value of the pretreatment albumin to globulin ratio in predicting long-term mortality in breast cancer patients, Am. J. Surg. **206**, 764 (2013).

[17] N. A. Alabkal, E. K. Metwally, M. H. Elnagdi, F. I. Aldosery, and N. S. Abbas, Quantitative analysis of components of heroin seized in Kuwait by gas chromatography/mass spectrometry, Phys. Rev. E **93**, 042303 (2016).

[18] E. Paleček and V. Dorčák, Label-free electrochemical analysis of biomacromolecules, Appl. Mater. Today **9**, 434 (2017).

[19] J. Mitchell, T. C. Chandrasekera, M. L. Johns, L. F. Gladden, and E. J. Fordham, Nuclear magnetic resonance relaxation and diffusion in the presence of internal gradients: The effect of magnetic field strength, Phys. Rev. E **81**, 026101 (2010).

[20] M. Atmaca, H. Yildirim, S. Yilmaz, N. Caglar, O. Mermi, M. G. Gurok, Y. Kekilli, and H. Turkcapar, ^{1}HMRS results of hippocampus in the patients with obsessive-compulsive disorder before and after cognitive behavioral therapy, Int. J. Psychiatry Clin. Pract. **19**, 285 (2015).

[21] Z. Wei, J. Yang, Y. Chen, Y. Lin, and Z. Chen, Line broadening interference for high-resolution nuclear magnetic resonance spectra under inhomogeneous magnetic fields, J. Chem. Phys. **142**, 134202 (2015).

[22] D. Bartusik, D. Aebisher, and B. Tomanek, A review of new approaches in Her-2 targeting and ^{1}H MRI application, Med. Chem. Res. **24**, 1365 (2014).

[23] M. C. Beard, G. M. Turner, and C. A. Schmuttenmaer, Measurement of electromagnetic radiation emitted during rapid intramolecular electron transfer, J. Am. Chem. Soc. **24**, 255 (2016).

[24] L. V. Wang and J. Yao, A practical guide to photoacoustic tomography in the life sciences, Nat. Methods **13**, 627 (2016).

[25] Y. Zhao, C. Chen, H. Liu, S. Yang, and D. Xing, Time-resolved photoacoustic measurement for evaluation of viscoelastic properties of biological tissues, Appl. Phys. Lett. **109**, 203702 (2016).

[26] N. Hao and A. Arbabian, Stepped-frequency continuous-wave microwave-induced thermoacoustic imaging, Appl. Phys. Lett. **104**, 224104 (2014).

[27] S. I. Denisov, T. V. Lyutyy, B. O. Pedchenko, and O. M. Hryshko, Induced magnetization and power loss for a periodically driven system of ferromagnetic nanoparticles with randomly oriented easy axes, Phys. Rev. B **94**, 024406 (2016).

[28] S. C. Sahu, V. Simplaceanu, Q. Gong, N. T. Ho, F. Tian, J. H. Prestegard, and C. Ho, Insights into the solution structure of human deoxyhemoglobin in the absence and presence of an allosteric effector, Biochemistry **46**, 9973 (2007).

[29] C. Y. Li, E. A. Hemmig, J. Kong, J. Yoo, S. Hernández-Ainsa, U. F. Keyser, and A. Aksimentiev, Ionic conductivity, structural deformation and programmable anisotropy of DNA origami in electric field, ACS Nano **9**, 1420 (2015).

[30] X. F. Zhang, P. F. Guan, and X. L. Dong, Multidielectric polarizations in the core/shell co/graphite nanoparticles, Appl. Phys. Lett. **96**, 223111 (2010).

[31] B. Gross, On the theory of dielectric loss, Phys. Rev. **59**, 748 (1941).

[32] G. D. Watkins, Motion of Mn++ cation vacancy pairs in NaCl: Study by electron spin resonance and dielectric loss, Phys. Rev. **113**, 91 (1959).

[33] G. B. Dudley, R. Richert, and A. E. Stiegman, On the existence of and mechanism for microwave-specific reaction rate enhancement, Chem. Sci. **46**, 2144 (2015).

[34] E. A. Guggenheim, The computation of electric dipole moments, Trans. Faraday Soc. **47**, 573 (1955).

[35] S. Shahriari, A. Mandanici, L. M. Wang, and R. Richert, Dynamics of glass-forming liquids. VIII. Dielectric signature of probe rotation and bulk dynamics in branched alkanes, J. Chem. Phys. **121**, 8960 (2004).

[36] U. Kaatze, Complex permittivity of water as a function of frequency and temperature, J. Chem. Eng. Data **34**, 371 (1989).

[37] See Supplemental Material at http://link.aps.org/supplemental/10.1103/PhysRevApplied.10.024044 for the effects of blood oxygen on microwave absorption, pumped-in-oxygen experiments *in vivo*, spatial resolution of the system, and frequency response of the thermoacoustic signal.

[38] K. Okazaki, H. Hayase, T. Ichinose, H. Mitono, T. Doi, and H. Nose, Protein and carbohydrate supplementation after exercise increases plasma volume and albumin content in older and young men, J. Appl. Physiol. **107**, 770 (2009).

[39] H. Schmilovitz-Weiss, A. Tovar, M. Halpern, J. Sulkes, M. Braun, Y. Rotman, R. Tur-Kaspa, and Z. Ben-Ari, Predictive value of serum globulin levels for the extent of hepatic fibrosis in patients with chronic hepatitis B infection, J. Viral Hepat. **13**, 671 (2006).

[40] G. T. C. Ko, V. T. F. Yeung, J. C. N. Chan, F. C. C. Chow, J. K. Y. Li, W.-Y. So, L. W. W. Tsang, and C. Cockram, Plasma fibrinogen concentration in a Chinese population, Atherosclerosis **131**, 211 (1997).

[41] G. Sun, S. Vasdev, G. R. Martin, V. Gadag, and H. Zhang, Altered calcium homeostasis is correlated with abnormalities of fasting serum glucose, insulin resistance, and β-cell function in the newfoundland population, Diabetes **54**, 3336 (2005).

[42] K. Jia, C. Zhang, X. Huang, L. Wang, X. Hao, R. Mu, B. Pan, J. Zhang, W. Chen, N. Xu, G. Li, Y. Y. Ma, M. Ma, W. Guo, and H. Shang, Reference intervals of serum sodium, potassium, and chlorine in Chinese Han population and comparison of two ISE methods, J. Clin. Lab. Anal. **29**, 226 (2015).

[43] E. H. F. Mcgale, I. F. Pye, C. Stonier, E. C. Hutchinson, and G. M. Aber, Studies of the inter-relationship between cerebrospinal fluid and plasma amino acid concentrations in normal individuals, J. Neurochem. **29**, 291 (1977).

[44] J. Ivanisevic, D. Elias, H. Deguchi, P. M. Averell, M. E. Kurczy, C. H. Johnson, R. Tautenhahn, Z. Zhu, J. D. Watrous, M. Jain, J. H. Griffin, G. J. Patti, and G. Siuzdak, Arteriovenous blood metabolomics: A readout of intra-tissue metabostasis, Sci. Rep. **5**, 12757 (2015).

[45] B. Y. Glassberg, The arteriovenous difference in blood sugar content, Arch. Intern. Med. **46**, 605 (1930).

[46] J. Yao, L. Wang, J. M. Yang, K. I. Maslov, T. T. W. Wong, L. Li, C. H. Huang, J. Zou, and L. V. Wang, High-speed label-free functional photoacoustic microscopy of mouse brain in action, Nat. Methods **12**, 407 (2015).

[47] A. P. Jathoul, J. Laufer, O. Ogunlade, B. Treeby, B. Cox, E. Zhang, P. Johnson, A. R. Pizzey, B. Philip, T. Marafioti, M. F. Lythgoe, R. B. Pedley, M. A. Pule, and P. Beard, Deep *in vivo* photoacoustic imaging of mammalian tissues using a tyrosinase-based genetic reporter, Nat. Photonics **9**, 239 (2015).